SUPPORTING INFORMATION

Quantum dot opto-mechanics in a fully self-assembled nanowire

Michele Montinaro,[1] Gunter Wüst,[1] Mathieu Munsch,[1] Yannik Fontana,[2] Eleonora Russo-Averchi,[2] Martin Heiss,[2] Anna Fontcuberta i Morral,[2] Richard J. Warburton,[1] and Martino Poggio*,[1]

[1] *Department of Physics, University of Basel, Klingelbergstrasse 82, 4056 Basel - Switzerland*

[2] *Laboratoire des Matériaux Semiconducteurs, École Polytechnique Fédérale de Lausanne, 1015 Lausanne - Switzerland*

* E-mail: martino.poggio@unibas.ch

S1. MECHANICAL PROPERTIES OF THE NANOWIRE

We calculate the lowest order flexural vibrations and the induced dynamic strain of the nanowire (NW) using a finite element model (FEM) of the experimental system. We approximate the NW structure as an isotropic and homogeneous hexagonal prism of AlGaAs, with a density given by the average of the densities of the different GaAs and AlGaAs layers, each weighted according to its thickness (see main text). The dimensions of the NW as well as its length that is tightly glued to the Si substrate on a lateral facet are measured by scanning electron microscopy (SEM).

The FEM provides the eigenfrequencies of the NW flexural vibrations and the corresponding mode shapes. While a symmetric clamping of the NW would result in doubly degenerate vibrational modes, the asymmetry of the actual clamping geometry, i.e. with only one lateral facet in contact with the substrate, splits each mode into a doublet of flexural vibrations oriented either parallel or perpendicular to the Si surface, with the former having the lower eigenfrequency. Figure S1 shows the mode shape of the lowest four non-degenerate vibrations. The spectral separation between two non-degenerate modes in each doublet depends, aside from the nature of the clamping, on the symmetry of the NW geometry: a dilatation of the hexagonal cross-section by only 1% along one axis is enough to invert the spectral positions of the two modes.

As discussed in the main text, in this experiment we focus our attention on the lowest order perpendicular mode. This orientation is preferentially driven by the piezoelectric transducer attached to the sample, is more easily detected by the interferometer, and driving higher order modes requires higher mechanical excitation power or a more sensitive displacement detection. The calculation of the mode shape of the favored flexural mode $u_\perp(\boldsymbol{r})$ as a function of the position $\boldsymbol{r}$ allows us to determine the corresponding motional mass m at the NW free-end, according to the definition:

$$m \equiv \int \rho \left| u_\perp(\boldsymbol{r}) \right|^2 \, \mathrm{d}V, \tag{S1}$$

where the integral is calculated over the entire NW volume V, ρ is the NW density, which in our model does not depend on $\boldsymbol{r}$, and $u_\perp(\boldsymbol{r})$ is normalized so that its maximum value is unity[1]. The result is $m = (3.5 \pm 0.7) \times 10^{-15}$ kg, where the error is dominated by the measurement imprecision of the NW thickness.

The flexural vibrations produce a time-varying material strain in the NW, which translates into a dominant uniaxial stress along the NW growth direction ($[1\,\bar{1}\,1]$ in crystallographic notation). This oscillating material strain is responsible for the modulation of the QD emission energy, therefore it is important to evaluate its strength and its spatial distribution. For this purpose, it is necessary to determine the values of the Young's modulus E_Y and of the Poisson's ratio ν, which fully characterize the elastic properties of isotropic materials[2].

To our knowledge, for a GaAs/AlGaAs nanostructure grown along $\langle 1\,1\,1 \rangle$, E_Y has not yet been measured. The only reference is the value along this axis measured for bulk GaAs (141.2 GPa)[3]. For this reason, we initially set E_Y as a free parameter in our FEM, while calculating the NW eigenfrequencies. We then tune E_Y in the FEM until the calculated resonance frequency of the lowest perpendicular mode matches our experimentally measured value of 795.4 kHz. The corresponding Young's modulus is $E_Y = 153$ GPa, which is 8% larger than the aforementioned value measured for bulk GaAs. Possible reasons for this increase of the stiffness of our NW reside in its finite size and in its core-shell structure, which introduces an additional intrinsic material strain.

The Poisson's ratio expresses the relative strength of the strain tensor components. By setting an xyz reference system with $\hat{z}$ oriented along the NW growth direction, the strain tensor in our case assumes the following form:

$$\varepsilon_{ij} = \begin{bmatrix} \varepsilon_\perp & 0 & 0 \\ 0 & \varepsilon_\perp & 0 \\ 0 & 0 & \varepsilon_\parallel \end{bmatrix}. \tag{S2}$$

In this reference system, the Poisson's ratio can be written as follows:

$$\nu = -\frac{\varepsilon_\perp}{\varepsilon_\parallel}. \tag{S3}$$

Signorello et al.[4] have recently measured ν for Zinc-Blende GaAs/AlGaAs core-shell NWs grown along $\langle 1\,1\,1 \rangle$, as in our case, at a temperature of 100 K (see Table S1).

Once these fundamental parameters have been inserted into our FEM, we compute the strain distribution along the NW structure. Figure S1 shows in color scale $\varepsilon_\parallel$ for the lowest four non-degenerate flexural vibrations, for a NW free-end displacement of 1 nm. The largest strain is obtained at the clamped end of the NW, at the borders of its hexagonal cross-section perpendicular to the oscillation direction. The mode doublet described by the indices $n = 2$ and 3 results in a maximum strain at the clamped end that is a factor 6 larger than the value of the lower index doublet. As confirmed by the FEM analysis, flexural modes of even higher index result in a further increase of the strain at the clamped end. Improvements in the detection of these higher modes should provide an opto-mechanical coupling parameter increased as

Parameter	Value	Unit
ν	0.16 ± 0.04	
a	-8.6 ± 0.7	eV
d	-5.2 ± 0.7	eV

Table S1. Electro-mechanical material parameters. The values have been measured for Zinc-Blende GaAs/AlGaAs core-shell NWs grown along $\langle 1\,1\,1 \rangle$, at a temperature of 100 K. Taken from Ref. 4.
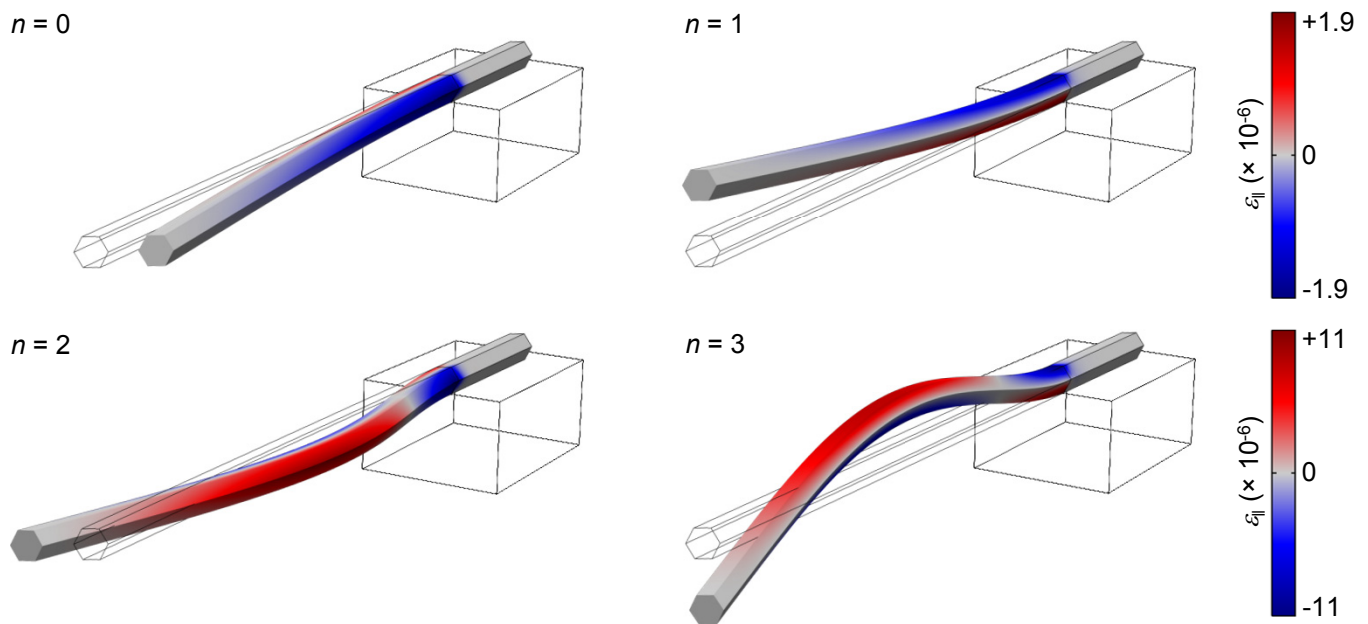
Figure S1. FEM of the NW mechanical properties. Each subfigure shows the mode shape of the lowest four non-degenerate vibrations, n being the mode index. The color scale is proportional to the component $\varepsilon_\parallel$ of the material strain in the NW, for a 1-nm displacement of its free end.

the strain. However, the coupling rate λ defined in the main text also depends on the NW's zero-point motion $x_{\mathrm{ZPF}} = \sqrt{\hbar/(2 m_n \Omega_n)}$. While the mode motional mass m_n does not depend in our geometry on n, the mode resonance frequency Ω_n increases with n, by a factor 6 for the second order doublet with respect to the first one. This dependence implies an increase of λ by a factor 2 (or bigger) for the second order (or higher) flexural modes of the NW.

S2. EFFECT OF STRAIN ON THE EXCITON TRANSITION ENERGY

The application of mechanical strain to the NW alters the lattice constant and the symmetry of the solid. These effects, in turn, cause significant changes in the electronic band structure that manifest themselves in the optical properties. The hydrostatic and shear components of the strain both contribute to such opto-mechanical coupling, with a weight given by their respective deformation potential, conventionally indicated as a for the hydrostatic deformation and d for the shearing induced by a stress along $\langle 1\,1\,1\rangle$[5,6]. The aforementioned work of Signorello *et al.*[4] has obtained these deformation potentials for NWs similar to ours (but without embedded QDs); the measured values are reported in Table S1.

The brightest exciton transition in our QDs concerns the conduction and the heavy-hole bands, each responding in a different way to the applied strain. The variation of the energy gap between these bands ($\Delta E^{\mathrm{C\text{-}HH}}$) under mechanical excitation can be connected to the strain

component $\varepsilon_\parallel$ through the following model[5]:

$$\Delta E^{\mathrm{C\text{-}HH}} = \left[(1 - 2\nu)\,a + \frac{1}{\sqrt{3}}(1 + \nu)\,d\right]\varepsilon_\parallel. \qquad (S4)$$

From the FEM of the NW, we extract the profile of $\varepsilon_\parallel$ along $\hat{z}$ corresponding to the lowest order perpendicular mode, for a given displacement of the NW free end. The graph in Fig. S2 shows such a plot for $\varepsilon_\parallel$ at 10 nm below the NW surface, a distance where the QDs best coupled to strain are located. The red spot, in particular, marks the position where the QDs analyzed in the main text are placed, $2.0\pm0.3\,\mu$m away from the clamped edge of the NW. Inserting the value of $\varepsilon_\parallel$ at the QD position into the Eq. S4, we obtain a displacement-dependent energy shift of $13 \pm 2\,\mu$eV/nm. Though this estimation does not take into account the detailed QD band structure, the value we have found is close to our experimental result ($9.9 \pm 0.7\,\mu$eV/nm), therefore confirming the strain-dependence of the band structure as the dominant coupling mechanism.

S3. DISTRIBUTION OF THE EXCITON ENERGY SHIFTS

We analyze the distribution of energy shifts of PL lines from QDs located in the same position along the NW length (within the laser detection spot), and emitting in a spectral range of 30 meV centered around 1.860 eV. This relatively narrow energy window restricts our analysis to QDs with similar size and composition. We consider the
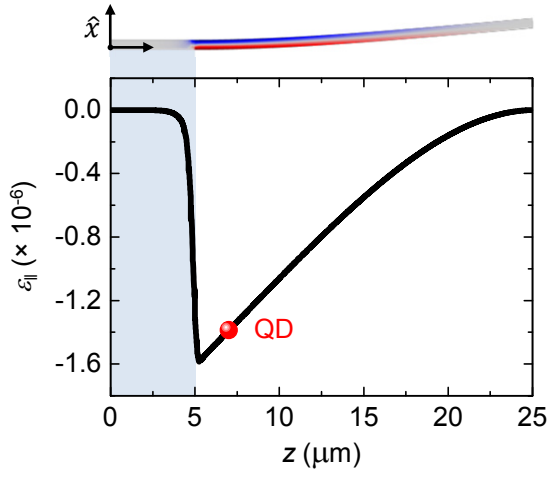
Figure S2. Strain profile along $\hat{z}$. The strain component $\varepsilon_{\parallel}$ at 10 nm below the NW surface is plotted for the NW free-end displaced through $u_{\perp}$ by 1 nm along $\hat{x}$. The shaded area from $z = 0$ to $z = 5\,\mu$m marks the region of the NW which is clamped to the substrate. The red spot at $z = 2.0 \pm 0.3\,\mu$m from the edge of the clamped region marks the position where the QDs analyzed in the main text are located. The upper inset shows the mode shape in consideration, with the strain amplitude in color scale as in Fig. S1.

energy shift induced in the QDs by a resonant mechanical excitation of the NW. In order to exclude the effect of asymmetric energy modulation, due to the different response of the QD band structure under compressive or tensile stress[4,7], we consider energy shifts only towards higher energies. The distribution of the data is plotted in Fig. S3(a).

The experimental result is compared to two different models for the spatial distribution of the QDs in the shell of the NW. The first model, illustrated in Fig. S3(b), assumes QDs located at the apexes of the NW hexagonal cross-section. The histogram in Fig. S3(c), instead, results from a model of QDs uniformly distributed along the shell perimeter.

The experimental distribution conforms more closely to the model of QDs located at the apexes of the cross-section. Though not conclusive, this analysis lends support to the interpretation of the QD spatial distribution in our NW structures originally given by Heiss *et al.*[8] and recently confirmed by Fontana *et al.*[9]. The observed deviations from such a model can be explained as weak fluctuations of size and composition of the analyzed QDs[10], and to different distances from the center of the cross-section.

S4. INTERFEROMETRIC DISPLACEMENT DETECTION

We use a 780-nm laser interferometer to detect the displacement of the NW free-end. Due to the low finesse of our cavity, the interferometer fringe as a function of the
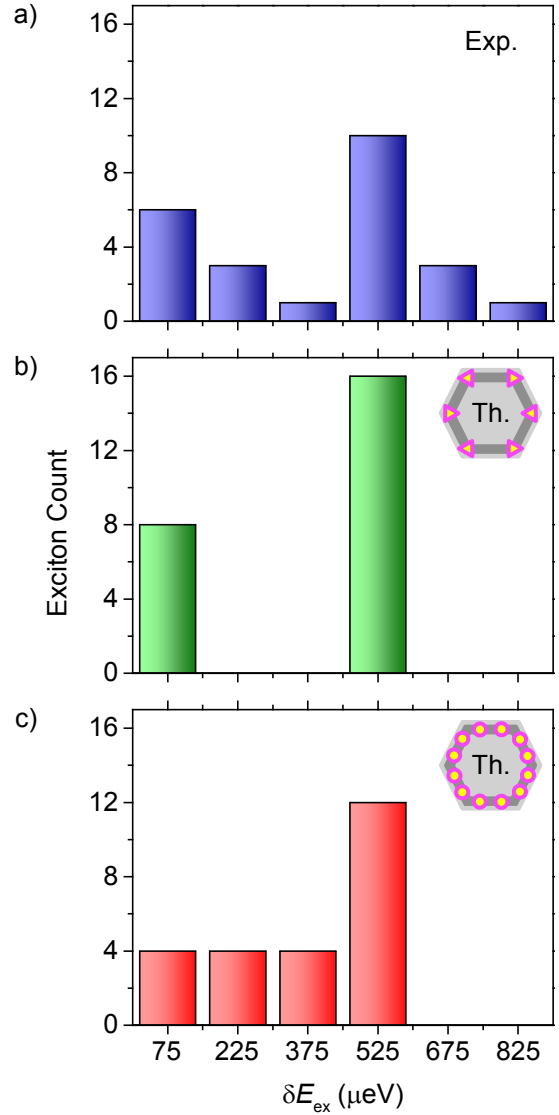
Figure S3. Distributions of energy shifts. (a) Experimental distribution of energy shifts for QDs emitting within a 30-meV spectral range and located at the same position along the NW length. (b) Model distribution for QDs located at the apexes of the NW shell. (c) Model distribution for QDs uniformly distributed along the shell perimeter. The two model distributions are normalized to the total exciton count of the experimental analysis.

cavity length or of the laser wavelength is well approximated by a sinusoid. The NW oscillation modulates the interferometer response in a small range around the fringe average, where the response becomes linear. We stabilize the interferometer in this linear regime, by controlling the laser wavelength via a PID feedback loop.

The cavity free spectral range measures $(2.6 \pm 0.1) \times 10^{-13}$ m, from which we derive a cavity length of 118 ± 5 cm. Measurements of the NW displacement are calibrated by an accurate determination of the laser wavelength. In order to double-check this calibration, we mea-
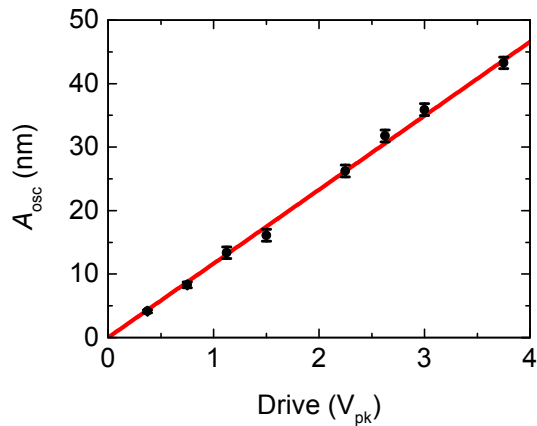
Figure S4. Interferometer test. Amplitude of the positioning stage displacement oscillation at 117 Hz as a function of the amplitude of the drive voltage, measured at a temperature of 4.2 K. The error bars correspond to the peak-to-peak amplitude of the interferometric noise. The red line is a linear fit, from which we extract a conversion factor of 11.6 ± 0.1 nm/V.

sure the displacement amplitude A_{osc} of the positioning stage along $\hat{x}$, while the stage is driven by a low-frequency oscillation (117 Hz). As shown in Fig. S4, the measurement is repeated for several drive voltages in order to extract, through a linear fit, a conversion factor for the piezoelectric positioning stage equal to 11.6 ± 0.1 nm/V. The entire procedure is repeated with the interferometer aligned to a variety of different positions on the yz plane, including the position of the NW free end. The values measured using our interferometer are close to the specifications of the positioning stage, which provide a rough conversion factor of 8 nm/V.

S5. DISPLACEMENT, FORCE, AND STRAIN SENSITIVITIES

The sensitivity of the QDs in our system to the resonant vibration of the NW could be used to reveal displacement variations due to the application of electrical or magnetic forces or to a change of the NW mass.

We estimate the sensitivity of our apparatus as a displacement transducer and as a force or strain detector. To this purpose, we first measure, for a QD emission line, the intrinsic fluctuation in time of the photon count in a narrow spectral bin around the transition energy E_{ex}^0. The amplitude of such fluctuation depends on the bin size and on the integration time τ. An external force applied to the NW produces, through the deformation potential coupling, a variation of the QD photon count in a given spectral interval. For such a force to be detectable, the induced photon count variation has to be bigger than the intrinsic fluctuation. This count variation is in turn a direct consequence of the emission energy modulation, whose amplitude δE_{ex} can be calculated through the model described in the main text. From the

opto-mechanical coupling parameter $\frac{\partial E_{\text{ex}}}{\partial x}\big|_{x=0}$ measured for QD 2, we are then able to convert the emission energy modulation into a root-mean-squared displacement x_{rms} of the NW free-end. Finally, by multiplying such displacement to the square root of τ, we obtain a displacement sensitivity ≈ 3 nm Hz$^{-1/2}$. Note that this result is limited, in particular, by the resolution of our spectrometer, equal to $60\,\mu$eV. On the other hand, the sensitivity could be improved by 4 orders of magnitude by means of resonant laser spectroscopy[11].

The applied force is proportional to the NW displacement x_{rms} through the spring constant $k = m\Omega_0^2 = 90 \pm 20$ mN/m. Therefore we are able to estimate a force sensitivity ≈ 300 pN Hz$^{-1/2}$.

Our setup is also sensitive to strain variations in the NW. The finite element model described in Section S1 relates the strain to the NW displacement. It is then possible to express a strain sensitivity of our setup, $\approx 5 \times 10^{-6}$ strain Hz$^{-1/2}$. This result is of the same order of the sensitivity recently estimated for strain-mediated coupling of a diamond cantilever to the spin of an embedded nitrogen-vacancy center[12].

REFERENCES

(1) Hauer, B. D.; Doolin, C.; Beach, K. S. D.; Davis, J. P. *Ann. Phys.* **2013**, *339*, 181–207.

(2) Cleland, A. N. *Foundations of Nanomechanics*; Eds. Springer: Berlin, 2003.

(3) Brantley, W. A. *J. Appl. Phys.* **1973**, *44*, 534–535.

(4) Signorello, G.; Karg, S.; Björk, M. T.; Gotsmann, B.; Riel, H. *Nano Lett.* **2013**, *13*, 917–924.

(5) Chandrasekhar, M.; Pollak, F. H. *Phys. Rev. B* **1977**, *15*, 2127–2144.

(6) Van de Walle, C. G. *Phys. Rev. B* **1989**, *39*, 1871–1883.

(7) Bryant, G. W.; Zieliński, M.; Malkova, N.; Sims, J.; Jaskólski, W.; Aizpurua, J. *Phys. Rev. B* **2011**, *84*, 235412.

(8) Heiss, M.; Fontana, Y.; Gustafsson, A.; Wüst, G.; Magen, C.; O'Regan, D. D.; Luo, J. W.; Ketterer, B.; Conesa-Boj, S.; Kuhlmann, A. V.; Houel, J.; Russo-Averchi, E.; Morante, J. R.; Cantoni, M.; Marzari, N.; Arbiol, J.; Zunger, A.; Warburton, R. J.; Fontcuberta i Morral, A. *Nature Mater.* **2013**, *12*, 439–444.

(9) Fontana, Y.; Corfdir, P.; Van Hattem, B.; Russo-Averchi, E.; Heiss, M.; Sonderegger, S.; Magen, C.; Arbiol, J.; Phillips, R. T.; Fontcuberta i Morral, A. *arXiv:1406.0163*, **2014**.

(10) Jöns, K. D.; Hafenbrak, R.; Singh, R.; Ding, F.; Plumhof, J. D.; Rastelli, A.; Schmidt, O. G.; Bester, G.; Michler, P. *Phys. Rev. Lett.* **2011**, *107*, 217402.

(11) Kuhlmann, A. V.; Houel, J.; Ludwig, A.; Greuter, L.; Reuter, D.; Wieck, A. D.; Poggio, M.; Warburton, R. J. *Nature Phys.* **2013**, *9*, 570–575.

(12) Ovartchaiyapong, P.; Lee, K. W.; Myers, B. A.; Bleszynski Jayich, A. C. *arXiv:1403.4173*, **2014**.